Pumping effect of heterogeneous meniscus formed around spherical particle

Hayate Nakamura, Tetsuya Ogawa, Motochika Inoue, Takuma Hori, Lizhong Mu, Harunori Yoshikawa, Farzam Zoueshtiagh, Georg Dietze, Takahiro Tsukahara, Ichiro Ueno

Pumping effect of heterogeneous meniscus formed around spherical particle

Hayate Nakamura[a], Tetsuya Ogawa[a], Motochika Inoue[a], Takuma Hori[b], Lizhong Mu[c], Harunori N. Yoshikawa[d,*], Farzam Zoueshtiagh[e], Georg Dietze[f], Takahiro Tsukahara[g,h], Ichiro Ueno[g,h,*]

[a] *Division of Mechanical Engineering, Graduate School of Science and Technology, Tokyo University of Science. 2641 Yamazaki, Noda, Chiba 278-8510, Japan*
[b] *Division of Advanced Mechanical Systems Engineering, Institute of Engineering, Tokyo University of Agriculture and Technology. 2-24-16 Koganei City, Naka Town, Tokyo 184-8588, Japan*
[c] *Key laboratory of Ocean Energy Utilization and Energy Conservation of Ministry of Education, School of Energy and Power Engineering, Dalian University of Technology, China*
[d] *Université Côte d'Azur, CNRS, Institut de Physique de Nice, France*
[e] *Université Lille, CNRS, ECLille, ISEN, Univ. Valenciennes, UMR 8520 - IEMN, F-59000 Lille, France*
[f] *Université Paris-Sud, CNRS, Lab. FAST, Bât. 502, Campus Univ., Orsay, F-91405, France*
[g] *Department of Mechanical Engineering, Faculty of Science and Technology, Tokyo University of Science. 2641 Yamazaki, Noda, Chiba 278-8510, Japan*
[h] *Research Institute for Science and Technology (RIST), Tokyo University of Science. 2641 Yamazaki, Noda, Chiba 278-8510, Japan*

Abstract

Hypothesis: A disturbance such as a microparticle on the pathway of a spreading droplet has shown the tremendous ability to accelerate locally the motion of the macroscopic contact line (Mu *et al.*, J. Fluid Mech. 830, 2017) [1]. Although this ability has been linked to the particle-liquid interaction, the physical mechanisms behind it are still poorly understood despite its academic interest and the scope of numerous industrial applications in need of fast wetting.

Experiments: In order to better understand the mechanisms behind the particle-liquid interaction, we numerically investigate the pressure and velocity fields in the liquid film. The results are compared to experiments assessing the temporal shape variation of the liquid-film meniscus from which pressure difference around

*Corresponding author
Email addresses: Harunori.YOSHIKAWA@univ-cotedazur.fr (Harunori N. Yoshikawa), ich@rs.tus.ac.jp (Ichiro Ueno)

the particle is evaluated.

Findings: The particle-induced acceleration of the film front depends both on the shape of the meniscus that forms around the particle foot and the liquid "reservoir" in the film that can be pumped thanks to the presence of the particle. The study validates the presence of three stages of pressure difference between the upstream and downstream regions of the meniscus around the particle, which leads to the local acceleration/deceleration of the macroscopic contact line. We indicate that asymmetric meniscus around the particle foot produces a net pressure force driving liquid and accelerating the liquid-film front.

Keywords: dynamic wetting, meniscus, capillary

2010 MSC: 00-01, 99-00

---

1. Introduction

Many natural systems exploit the wetting of their surfaces in various aspects. For example, lotus leaves repel water droplets by their microstructures [2]; nepenthes rafflesianas profit of quick liquid transport thanks to their unique surface structures [3]; water-walking insects take postures that deform the free surface and enable them to leap over menisci [4]. Wetting also finds its importance in numerous industrial fields. Efficient heat transfer in heat pipes requires enhanced wetting of their inner surfaces by working fluids. The functioning of a micro-total analysis system (μ-TAS) may fully depend on the wetting phenomena in microfluidic channels and involved elements [5]. For instance, the transport of a small amount of liquid into a small inspection region of μ-TAS is realized by chemical [6, 7] or physical functionalization of surfaces [8] where controlled wetting is of utmost importance.

Owing to its importance, numerous studies on wetting have been reported. Liquid spreading on a solid surface can be characterized by the behavior of a contact line (CL), which is a junction of solid, liquid, and gas phases. The dynamics of a CL can be characterized by the spreading parameter, $S = \gamma_{\mathrm{SG}} -$

$\gamma_{SL} - \gamma$, where γ_{SG}, γ_{SL} and, γ are the interfacial tensions of solid-gas, solid-liquid and liquid-gas interfaces, respectively [9]. A contact line can be pinned onto a solid surface under $S < 0$ to form a static contact angle predicted by Young's equation [10]. A CL can advance under $S > 0$ to extend the wetted area of surface. Focusing on this phenomenon, Hoffman performed experiments of pushing silicone oil in a glass tube with a piston [11]. The correlation between the contact angle θ and the capillary number $\mathrm{Ca} = \mu U/\gamma$ was derived; here, μ and U are the dynamics viscosity of the liquid and the velocity of the CL, respectively. The capillary number is an important parameter for estimating the effects of viscous stress on liquid spreading.

The correlation between the spreading radius R and the spreading time t of liquid film on a smooth horizontal substrate can be expressed as $R \sim t^a$ [12, 13, 14]. Here, a is an exponent that depends on the dominant force acting on the liquid film; $a = 1/10$ and $1/8$ in the regimes of the interfacial-force dominant [13] and the gravity-dominant [12], respectively. In particular, the parameter becomes $a = 1/7$ in the one-dimensional spreading when surface tension is dominant. In the case of rough surfaces, it was indicated that the roughness enhances the wettability under $S > 0$ [15]. Microstructures of solid surfaces change the wetting behavior significantly [16, 17, 18, 19, 20]. The coupled effects of surface chemical properties and surface topology on the exponent were investigated [7].

Recently, the dynamics of an advancing CL interacting with spherical particles placed on a horizontal substrate was investigated [1, 21]. It was shown that the CL can undergo a large acceleration up to 10 times faster than in the absence of particles. Mu *et al.* [1] attributed this behavior to the curvature of the meniscus formed around spherical particles and showed that the observed large velocities can be explaneed by their theoretical model based on the Cox's law [22]. Mu *et al.* [23] extended the experimental studies of Mu *et al.* [1] and Kondo *et al.* [21] but with different particles in cylindrical and triangular prism shapes. They found that spherical particles caused the largest acceleration. They also showed that the sequential arrangement of microstructures enables

a control over the direction of liquid transport, which would constitute a novel efficient alternative to existing liquid transport techniques [24].

In this paper, we perform numerical simulations of the interaction between a CL and a single particle by a numerical code based on the InterFoam solver of the open-source software OpenFOAM. The goal is to elucidate the details of the local flow characteristics in the wetting process and unravel the physical mechanisms behind the acceleration of the CL. The behavior of CL predicted by the simulations are first compared with experiments to validate our numerical code. The velocity field and pressure distribution obtained by the simulations are then examined. Based on the computational results, the physical mechanism responsible for the CL acceleration is unraveled.

2. Methods

2.1. Numerical simulations

The open-source solver for computational fluid dynamics, OpenFoam (ver. 5.0), is used to carry out the present numerical simulations. The free-surface modeling technique of the volume of fluid [25] is used to track the gas-liquid two-phase flow. The governing equations for the simulations are:

$$\nabla \cdot \boldsymbol{U} = 0 \tag{1}$$

$$\frac{\partial \rho \boldsymbol{U}}{\partial t} + \nabla \cdot (\rho \boldsymbol{U}\boldsymbol{U}) = -\nabla p + \nabla \cdot \boldsymbol{\tau} + \rho \boldsymbol{g} + \boldsymbol{F}_{\mathrm{SV}} \tag{2}$$

$$\frac{\partial \alpha}{\partial t} + \nabla \cdot (\alpha \boldsymbol{U}) + \nabla \cdot (\boldsymbol{U}_{\mathrm{r}} \alpha \, (1 - \alpha)) = 0. \tag{3}$$

Equations (1)-(3) are, respectively, the continuity equation of incompressible flows, the Navier-Stokes equation, and an advection equation of volume function α. The symbols $\boldsymbol{U}$, p, $\boldsymbol{\tau}$, $\boldsymbol{F}_{\mathrm{SV}}$, $\boldsymbol{U}_{\mathrm{r}}$ represent velocity, pressure, viscous stress, force induced by the interfacial tension, and relative velocity between liquid and gas phases, respectively. The volume fraction α of the liquid phase takes

values of 1 and 0 when an computational cell is fully occupied by liquid and gas, respectively, and takes in-between values when an interface is present in the cell. Solving the advection equation enables to track the interface. Note that in order to counteract the numerical diffusion, a compression velocity is used. We define $\alpha = 0.5$ isosurface as the liquid-gas interface. The stress due to the interfacial tension is described by $\boldsymbol{F}_{\mathrm{SV}} = \gamma\kappa\boldsymbol{n} = \gamma\kappa\boldsymbol{\nabla}\alpha/\|\boldsymbol{\nabla}\alpha\|$ by continuum surface force method [26], where κ and $\boldsymbol{n}$ are the curvature of the interface and the unit normal vector of the interface pointing to the gas phase, respectively.

The computational domain is shown in Fig. 1. The length and grid number of the domain are $(L_x,\ L_y,\ L_z)$ [μm] = (300, 80, 300) and $(N_x,\ N_y,\ N_z)$ = (150, 40, 150), respectively. The origin of the coordinate system is set on the substrate surface at the upstream edge of the computational domain. No-slip and no-penetration conditions are imposed at the substrate surface (x, $y = 0$, z). The top plane (x, $y = L_y$, z) and the side planes ((x, y, $z = 0$); (x, y, $z = L_z$)) are set to mirror boundaries. A spherical solid boundary representing a particle of diameter $D_{\mathrm{p}} = 50$ μm is positioned at the center of the substrate ($x_{\mathrm{p}} = 150$, $y_{\mathrm{p}} = 25$, $z_{\mathrm{p}} = 150$) μm. The wettability of the substrate and that of the particle are prescribed by contact angles $\theta_{\mathrm{s}} = 5^\circ$ and $\theta_{\mathrm{p}} = 20^\circ$, respectively. The advancing/receding contact angles for the substrate and particles are set to be 0° and 10°, and 10° and 30°, respectively. We set the physical properties of liquid and gas as those of 2-cSt silicone oil and air used in the experiments; the surface tension, density and kinematic viscosity of the liquid are $\gamma = 1.83 \times 10^{-2}$ N/m, $\rho_{\mathrm{l}} = 873$ kg/m^3, $\nu_{\mathrm{l}} = 2.0 \times 10^{-6}$ m^2/s, and the density and kinematic viscosity of the gas are $\rho_{\mathrm{g}} = 1$ kg/m^3 and $\nu_{\mathrm{g}} = 1.48 \times 10^{-5}$ m^2/s, respectively. The gravitational acceleration is set to be constant at $g = 9.81$ m/s^2. At time $t = 0$ s, the liquid film starts to flow into the computational domain under the condition of $P_{\mathrm{inlet}} = 0$ from the inlet of height $h_{\mathrm{inlet}} = 20$ μm at the $x = 0$ boundary. The capillary number of the liquid flow is small, *e.g.*, $\mathrm{Ca} = 3.01 \times 10^{-4}$ just before the particle start to be wetted, but larger than in the experiments (Sec. 2.2 and Ref. [1]) in order to reduce the time for flow computation. Kondo *et al.*[21] indicated that the ratio of the maximum

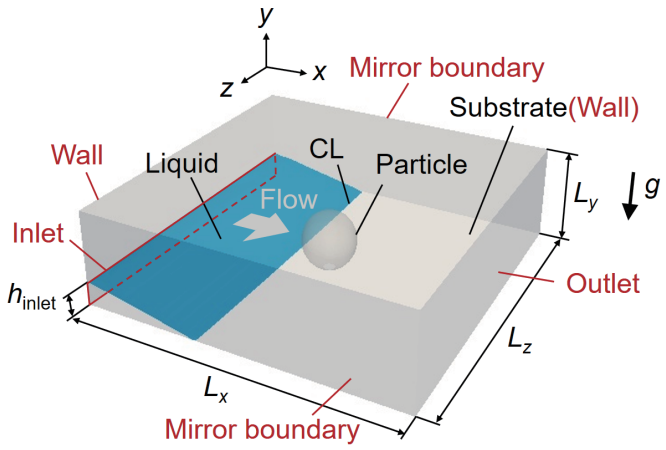

Figure 1: Computational domain of spreading liquid film on horizontal substrate with a single particle.

velocity of the contact line to the velocity just prior to the interaction with the particle on the substrate become drastically smaller as increasing Ca. It was indicated that the maximum velocity decreases accompanying with the particle sucked to the bulk of the droplet after the contact with the contact line of the droplet. It must be noted that such trend was obtained in the system with the mobile particle just settled on the substrate. In the present simulation, we employ the particle fixed to the substrate, thus the trend observed by Kondo *et al.*[21] never takes place. Corresponding Reynolds number $\mathrm{Re} = U_0 D_\mathrm{p}/\nu$ and Ohnesorge number $\mathrm{Oh} = \sqrt{\rho\nu^2/(\gamma D_\mathrm{p})} = \sqrt{\mathrm{Ca}/\mathrm{Re}}$ for the present simulation are $\mathrm{Re} = 7.89\times10^{-2}$ and $\mathrm{Oh} = 6.18\times10^{-2}$, respectively. Here U_0 is the velocity of the macroscopic contact line just prior to the contact with the particle. We limit ourselves to deal with the phenomenon under which the effect of inertia is negligible.

2.2. Experiment

Experiments are conducted to assay the similarity and the validity of the computational results. The setup, identical to that of Mu *et al.*[1], is illustrated in Fig. 2. For detailed description of the setup refer to Mu *et al.*[1] The test fluid

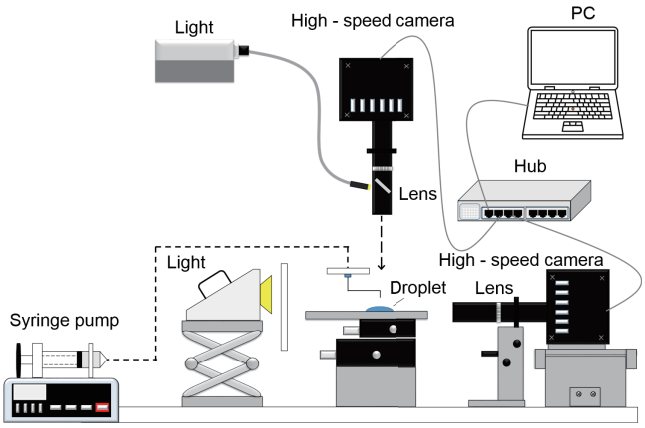

Figure 2: Experimental apparatus for observation of droplet spreading on substrate. Simultaneous observation from above and side is realized with synchronized two high-speed cameras.

is 2-cSt silicone oil (polydimethylsiloxane, KF-96L-2cSt, Shin-Etsu Chemical Co., Ltd.), with a density of $\rho = 873$ kg/m^3, a kinematic viscosity of $\nu = 2.00$ mm^2/s, and a surface tension of $\gamma = 18.3$ mN/m at 25 °C. A syringe pump (YPS-202, YMC Co., Ltd.) delivers a droplet of volume of 1.8 mm^3 through a needle tip coated with fluoride. The height of the needle tip from the substrate is set to 2.0 mm. The substrate is a silicon-wafer priory cleaned by acetone and then by plasma (PDC 32G, Harrick Plasma) for a duration of 10 minute before every experimental run. Spherical glass particles (Soda lime, Fuji Manufacturing Co., Ltd.) of diameter $D_\mathrm{p} = 200$ μm are used. The particle size here is larger than those used in the previous experiment [1] and in our numerical simulations in order to capture the gas-liquid interface with higher accuracy. The horizontal distance between the centers of the particle and the needle tip is 4.0 mm. The interaction between the liquid and the particle is monitored simultaneously from top and side by high-speed cameras (Fastcam Mini WX100, Photron Ltd.). The resolution in top and side views are 2.17 μm/pix and 0.77 μm/pix, respectively. The frame rates of both cameras are 50 frames per second (fps). A 100 W cold light (MegaLight 100, Moritex Corp.) is used for light source.

3. Results and discussion

3.1. Experiment

The spatio-temporal profiles of the liquid film interacting with a particle are derived from the videos captured by the high-speed cameras. The snapshot views in Fig. 3 (a, b) show the spreading behavior of the droplet near the particle in both views. We here define as t_0 [s] the moment at which the meniscus starts to envelop the particle observed from top. The velocity of the CL, U_{CL}, is obtained from video analysis. In order to evaluate U_{CL}, we apply the process as indicated in Fig. 4 in [1] to the successive images observed from the side. That is, we construct a space-time diagram along the substrate surface for tracking the position of the macroscopic contact line, $X_{\mathrm{CL}}(t)$, from the successive side-view images. The velocity U_{CL} is then the computed from the temporal evolution of $X_{\mathrm{CL}}(t)$. The capillary number just before interacting with particle corresponds to $\mathrm{Ca} \sim 3.7 \times 10^{-6}$. Under the present condition for the experiment, the Reynolds and Ohnesorge numbers are $\mathrm{Re} \sim 3.9 \times 10^{-3}$ and $\mathrm{Oh} \sim 3.1 \times 10^{-2}$, respectively. We thus neglect the inertia effect in the present system as [1]. The profiles of liquid film in the symmetry plane (*i.e.*, the plane $z = z_{\mathrm{p}}$) extracted from side-view images are shown in Fig. 3 (c). By monitoring the temporal evolution of the spatial profiles of the meniscus formed around the particle, we obtain the same tendency as that in the previous study using smaller spherical particles of diameter $D_{\mathrm{p}} = 50$ μm [1]. That is, when the spreading liquid film makes a contact with the particle, a concave meniscus, *i.e.*, a meniscus with negative curvature in the x-y plane, forms around the particle foot, as seen in Fig. 3 (b, c).

From meniscus profiles we evaluate the pressure difference Δp_{gl} between liquid and gas phases based on the stress balance at interface,

$$\Delta p_{\mathrm{gl}} := p_{\mathrm{g}} - p_{\mathrm{l}} = \gamma \left(\frac{\xi_{yy}}{\left(1 + \xi_y^2\right)^{3/2}} - \frac{1}{\xi \left(1 + \xi_y^2\right)^{1/2}} \right), \tag{4}$$

where p_{g}, p_{l} represent the pressures on the gas and liquid sides of the interface, respectively, and $x = \xi(t, y)$ is the meniscus profile in the symmetry plane. ξ_y

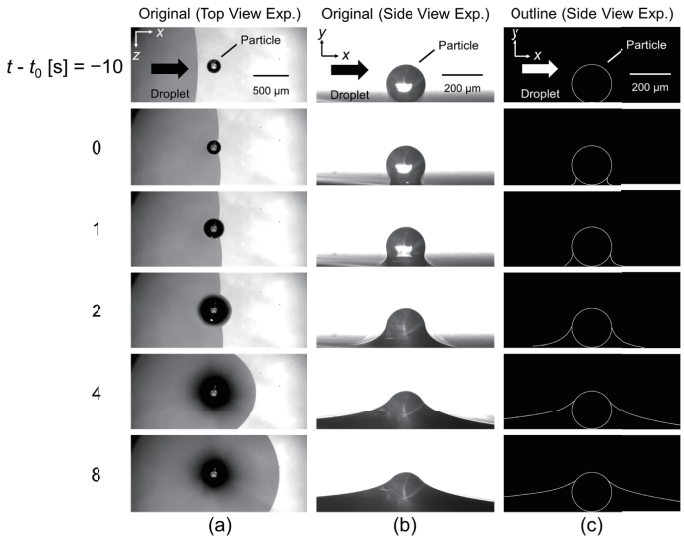

Figure 3: Meniscus formation around a particle of a diameter $D_\mathrm{p} = 200$ μm observed in an experiment. Images in top view (a) and in side view (b) and meniscus profiles (c) extracted from the side view images.

and ξ_{yy} stand for the first and second derivatives of ξ with respect to y. In Eq. (4), viscous stresses and gravity force are neglected, as both capillary and Bond numbers, Ca, Bo are small: $\mathrm{Ca} \sim 3.7 \times 10^{-6} \ll 1$ and $\mathrm{Bo} = \rho D_\mathrm{p}^2 g/\gamma \sim 1.87 \times 10^{-2} \ll 1$ in our experiment. The stress balance condition at the interface then takes the same form as the Young-Laplace equation. In Equation (4), we have also assumed that the azimuthal variation of meniscus shape around the particle is locally negligible at the upstream and downstream sides. This assumption is supported by the fact that the CL downstream of the meniscus remains circular throughout meniscus development as shown in Fig. 3 (a). We estimate Δp_gl for an observed meniscus by seeking a value of Δp_gl that produces the solution of Eq. (4) fitting the best the experimental profile. This evaluation of Laplace pressure is validated from numerical results (Appendix).

The temporal variation of velocity of the CL, U_CL are shown in Figure 4 (b). The net pressure difference (Fig. 4 (c)) between upstream and downstream of the particle is assessed from $\Delta p'^{(\mathrm{ud})} := p_\mathrm{l}^{(\mathrm{up})} - p_\mathrm{l}^{(\mathrm{down})} = \Delta p_\mathrm{gl}^{(\mathrm{up})} - \Delta p_\mathrm{gl}^{(\mathrm{down})}$

where superscripts (up) and (down) indicate 'upstream' and 'downstream' with respect to the particle, respectively. These figures show a rapid increase of U_{CL} at the beginning of meniscus formation (at $0 \leq t - t_0$ [s] ≤ 2.6), before a decrease (at $t - t_0$ [s] > 2.6) as the pressure difference drops. Here, U_{CL} hits maximum value slightly after the highest pressure difference $\Delta p'^{(\mathrm{ud})}$ is reached. This observation suggests that the pressure inside the meniscus is an important factor for the acceleration of the .

3.2. Simulation

Figure 5 shows numerical results of the spreading distance X_{CL} and the U_{CL} on the substrate with or without the particle. The spreading distance X_{CL} is defined as the CL position along the line of (x, $y = 0$, $z = z_{\mathrm{p}}$), and U_{CL} is approximated by central differences. As shown in Fig. 5, on the flat substrate without the particle, the simulations correctly reproduce the liquid film spreads by following Tanner's law [13], $X_{\mathrm{CL}} \propto t^{1/7}$ and $U_{\mathrm{CL}} \propto t^{-6/7}$. Similar to the experiments, the presence of the particle significantly alters the spreading of the liquid film: the velocity increases to reach a maximum value and then gradually decreases.

The theoretical analysis in the previous study [1] found that the meniscus formed around the particle plays an important role in the acceleration phenomenon. We now investigate in detail what happens within the meniscus based on our numerical simulations, as shown in Fig. 6. In our simulation, the liquid film rises up around the particle right after the interaction, and the meniscus with negative curvature of the interface is spontaneously formed, which is similar to our experimental results. At the initial stage of meniscus formation (*i.e.,* just after the liquid film contacts with the particle), the velocity on the meniscus surface exhibits an increase locally at the contact part ($t = 15.0$ ms). As the liquid film rises around the particle, the CL on the substrate spreads forward ($t = 17.0$ ms), and then decreases ($t = 19.0$ ms). Here, the interface shape of the liquid film in the x-y cross section is shown in Fig. 7 to discuss the detail of its time evolution. The inset shows the comparison of the CL angular

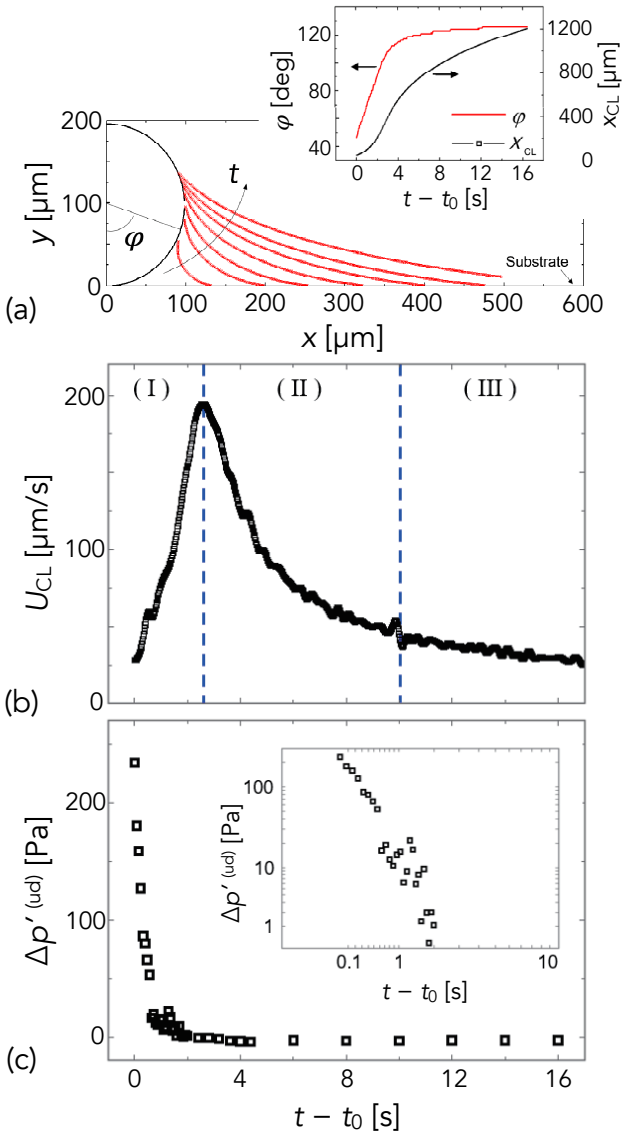

Figure 4: memo by IU:

I plan changing the figure for (a); temporal variations of the meniscus are also illustrated as Mu *et al.*(JFM 2017) in order to reflect the comment 4 by the reviewer1. What do you think? (a) Example of evaluating profiles of meniscus (red) formed around particle from experimental result. Inset: temporal variations of the contact-line positions along the particle, ϕ, and that along the substrate, X_{CL}. Temporal variations of (b) CL velocity U_{CL} and (c) evaluated pressure difference between menisci on upstream and downstream sides $\Delta p_{\mathrm{l}}^{\prime(\mathrm{ud})} := p_{\mathrm{l}}^{(\mathrm{up})} - p_{\mathrm{l}}^{(\mathrm{down})} = \Delta p_{\mathrm{gl}}^{(\mathrm{up})} - \Delta p_{\mathrm{gl}}^{(\mathrm{down})}$, where superscript (up) and (down) indicate 'upstream' and 'downstream', respectively.

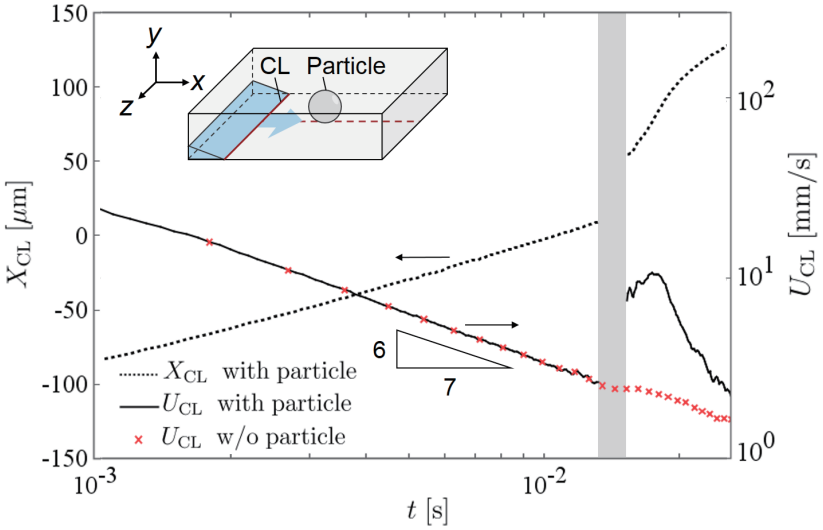

Figure 5: Temporal variations of the CL position X_{CL} and velocity U_{CL} on substrates. The CL position is derived on the line parallel to the x direction passing under the particle foot on the substrate as illustrated in inset. Note that the CL position is not well defined in the gray area, in which the CL is traveling around the particle foot.

position φ_{CL} around the particle and X_{CL}. Because the CL of the spreading liquid film keeps advancing downstream of the particle, the distance over which the meniscus connects the substrate to the particle becomes longer and longer, and this causes the meniscus curvature (in the x-y plane) to decrease in magnitude. Such trend qualitatively agrees with the experimental results [1]. We note the time scale of meniscus formation $\mathcal{O}(10^{-2}$ s) is different from that in the experiments $\mathcal{O}(1$ s), since the capillary number just in prior to the liquid contact with the particle in our simulation is larger than that in the experiment.

We monitor the temporal variation of the pressure distribution in the meniscus during its formation process, which is difficult to be observed in the experiment. Figure 8 illustrates the spatio-temporal variation of the pressure around the particle at different y. At $t = 15.0$ ms, the contact line makes a contact with the particle to form the meniscus. The lines that are almost parallel to the z axis at this instant are the contours of $\alpha = 0.5$ at each y position. Only

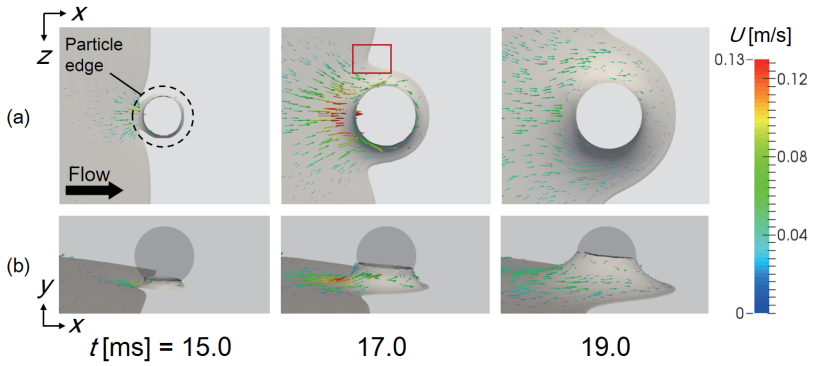

Figure 6: Meniscus formation around a particle of a diameter 50 μm observed in a simulation. Vectors indicate the velocity on the meniscus surface. Note that the particle periphery at the same level in y as the front of the meniscus is illustrated in (a) for the sake of visibility.

the liquid near the substrate touches the particle, the contour at $y = 0$ is deformed, and those at $y = 5$ and 10 exhibit almost straight shape. Due to the negative curvature of the liquid film to form the meniscus as aforementioned, the pressure in the meniscus around the partciel foot becomes negative ($y = 0$). As time elapses, the contact line along the particle surface rises to form larger meniscus, the contour becomes deforms at higher positions (see $y = 5$ at $t = 18$, and $y = 5$ and 10 at $t = 21$). As the meniscus develops around the particle, the absolute value of negative pressure becomes smaller in the meniscus because the curvature radius becomes larger as illustrated in Fig. 7. One finds that there exists negative gradient of the pressure around the particle in the x direction; the pressure in the upstream region against the particle becomes higher than the downstream region. This pressure gradient drives the liquid inside the meniscus toward the downstream side against the particle like a pump. It is obvious that the distribution of the pressure is symmetrical about the plane of $z = z_{\mathrm{p}}$. In the following we will discuss the pressure distribution in that plane.

As shown in Fig. 9 (a), the pressure inside the meniscus is lower than the atmospheric pressure at an initial stage ($t = 15.0$ ms). As the liquid film rises around the particle, the pressure inside the meniscus increases towards

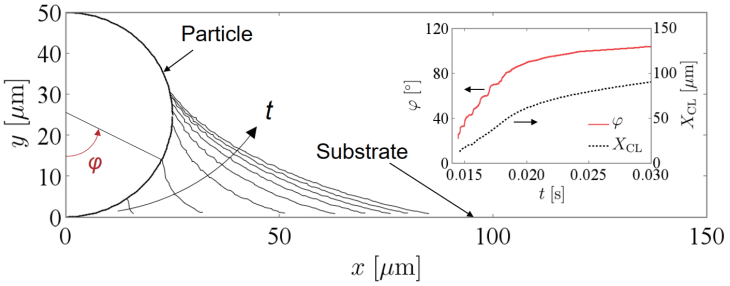

Figure 7: Temporal variation of meniscus profile around a particle on plane of $z = z_{\mathrm{p}}$ by numerical simulation. First profile corresponds to the meniscus surface at $t = 0.015$ s and the time interval between profiles is of 0.0002 s. Inset illustrates temporal variations of angular position φ_{CL} of the meniscus front on the particle and the position of CL on the substrate X_{CL}.

the atmospheric pressure because of the diminishing curvature caused by the ongoing advancement of the CL ($t = 15.0$ to 21.0 ms) as shown in Fig. 7 as well. At the same time, the pressure difference between upstream and downstream sides is generated inside the meniscus at the particle foot ($t = 18.0$ ms), and it eventually diminishes ($t = 21.0$ ms). These results can be also explaneed by assuming that the Young-Laplace equation (4) is applicable to dynamical wetting. As aforementioned, the pressure difference between the menisci on the upstream and downstream sides drives the liquid forward along the particle foot.

The time evolution of the pressure difference $\Delta p = p^{(\mathrm{up})} - p^{(\mathrm{down})}$ inside the menisci on the upstream and the downstream sides and the CL velocity U_{CL} are shown in Fig. 9 (b). Here, the pressures $p^{(\mathrm{up})}$ and $p^{(\mathrm{down})}$ are extracted at $\boldsymbol{x}_{\mathrm{up}}$ and $\boldsymbol{x}_{\mathrm{down}}$, corresponding to $(x,\ y,\ z)$ $[\mu\mathrm{m}] = (x_{\mathrm{p}} \pm 15,\ 2.5,\ z_{\mathrm{p}})$. The CL velocity after the encounter with the particle (marked by the gray region in panel 9 (b) can be roughly classified into three regions of (I) acceleration, (II) deceleration, and (III) convergence. The volume function α_{up} and α_{down} at the two points x_{up} and x_{down} are also shown in the upper graph of Fig. 9 (b), in order to show when the advancing contact line has reached the downstream evaluation point x_{down}. This happens at $t = 14.5$ ms. Before that instant, the pressure $p^{(\mathrm{down})}$ at $x = x_{\mathrm{down}}$ corresponds to the ambient gas pressure and thus

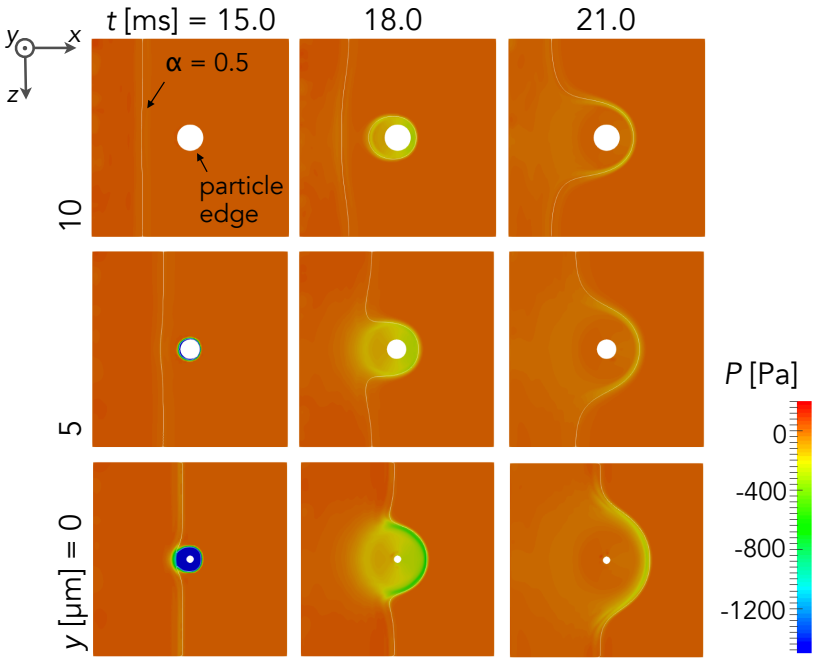

Figure 8: Spatio-temporal distributions of pressure at different height y.

the time trace of Δp carries the signature of $p^{(\mathrm{up})}$. This pressure decreases when the meniscus starts to form on the upstream side of the particle, producing the minimum in the Δp trace. Then, as the meniscus forms around the particle foot and reaches x_{down}, Δp becomes positive and reaches a maximum. This is due to the asymmetric nature of the meniscus, which displays a greater curvature on the downstream side. The CL velocity on the substrate reaches the maximum value slightly after it. From these results, we conclude that the meniscus plays a role as a 'pump' to suck a liquid from the bulk of the film and supply it behind the particle due to the pressure difference inside the meniscus between the front (upstream) and rear (downstream) of the particle.

In order to investigate the detailed behavior of the liquid inside the meniscus, the pressure, the absolute velocity U, and the velocities in x-, y- and z-directions in the liquid film around the particle on $(x,\ y,\ z) = (x_{\mathrm{p}},\ y,\ z)$ cross section are shown in Fig. 11. Initially the velocity in the x direction of the liquid

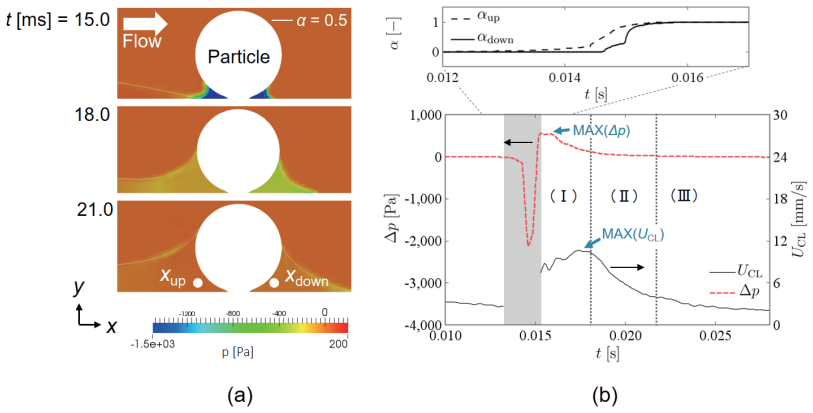

Figure 9: (a) Temporal variation of pressure around a particle on plane of $z = z_{\mathrm{p}}$. (b) Temporal variations of pressure difference between upstream (at x_{up} as shown in (a)) and downstream (x_{down}) sides in meniscus, and CL velocity U_{CL}. The monitoring points inside the meniscus on the upstream and downstream sides are defined as $\boldsymbol{x}_{\mathrm{up}}$ = (135, 2.5, 150) [μm], $\boldsymbol{x}_{\mathrm{down}}$ = (165, 2.5, 150) [μm], respectively. Top of (b) indicates the temporal variation of the volume fraction α measured at x_{up} (α_{up}) and at x_{down} (α_{down}). The position of CL on the substrate cannot be well defined in the gray area.

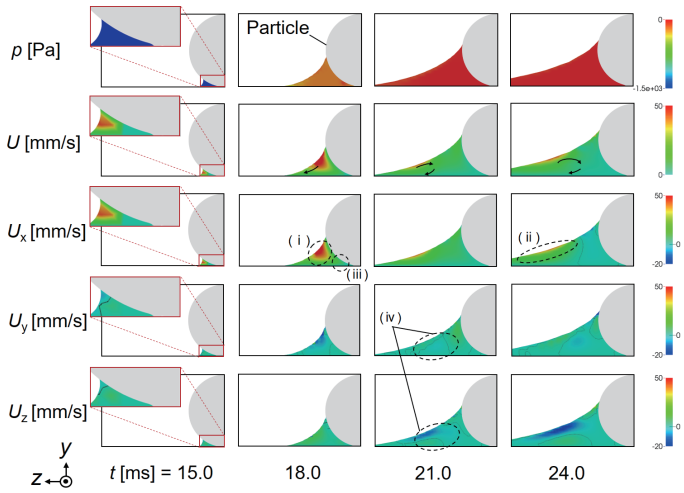

Figure 10: Spatial-temporal variations of pressure, absolute velocity, and velocity component in each direction inside the meniscus formed around the particle on plane of (x, y, z) = (x, y, z_{p}).

Figure 11: viscous dissipation??

film, U_x, develops in the vicinity of the gas-liquid interface near the contact line on the particle, and then the large U_x region transit to the z direction as the liquid film rises around the particle (region (i) $\rightarrow$ region (ii)). The small region near the particle foot (region (iii)) prevents the liquid to supply forward because of the viscous effect. The variation of the position where the velocity becomes maximum corresponds to the transition of the dominant driving force to 'pump' the liquid toward downstream region from the pressure difference within the meniscus in the main flow direction to the interfacial tension acting on the interface with the curvature (red square in Fig. 6 (a)). One finds that the distribution of U_x is almost the same as that of U, thus the pumping effect contributes the liquid transport almost along the x direction.

viscous dissipation??

4. Concluding remarks

The physical mechanism behind the local acceleration of the contact line of a spreading droplet due to its interaction with a microparticle as reported by Mu *et al.* [1, 23, 24] was investigated numerically and experimentally. The aim of the numerical simulations was to access the physical data such as the pressure and velocity fields in the liquid film forming around the particle that were not accessible experimentally. The experiments were used to validate the numerical simulations through the time-dependent shape taken by the meniscus around the particle's foot. Numerical simulations reproduce the experimental observations of an accelerating microscopic contact line around the particle. In particular, the simulations similarly show that the particle-liquid film interaction enables the microscopic contact line of a spreading of droplet to accelerate and overcome locally the commonly known power laws of Tanner or Lopez [12, 13, 14]. This result is of primary importance as it provides a numerical tool to predict the wetting dynamic of a substrate by a liquid with respect to topological conditions.

The simulations were limited to small capillary numbers $\mathrm{Ca} = \mu U_{\mathrm{CL}}/\gamma \sim \mathcal{O}(10^{-4})$ to $\mathcal{O}(10^{-6})$. In order to unravel the physics behind the contact line acceleration, a particular focus was made in studying the process of meniscus formation right after the contact of the contact line with the particle. Three regimes of behaviour for the contact line were identified: an accelerating, a decelerating, and a converging regime [21]. It is found that the characteristic time for the meniscus formation around the particle becomes of the order of $\mathcal{O}(10^{-2}$ s) which is much longer than that reported in the literature for the fully wetting of a smooth substrate by a liquid [27]. Furthermore, the relaxation of the Laplace pressure occurs within a long characteristic time of the order of $\mu D_{\mathrm{p}}/2\gamma \sim \mathcal{O}(10^{-6}$ s). This long characteristic time is linked to the significant limitation of the liquid within a liquid film. Indeed, the pressure difference between the upstream and downstream regions of the meniscus around the particle is behind the pumping mechanism that delivers the liquid from the bulk to the contact line behind the particle. Once the pressure difference vanishes the local

contact line around the particle decelerates till it is matched by the main contact line of the spreading droplet that follows the Tanner's law [13]. Those findings leads a comprehensive description of the enhancement of the droplet spreading on the microstructured solid surfaces [16, 17, 18, 19, 20]. We will apply these findings and the numerical simulations to optimize the wetting of a microstructured surface. It will, in particular, be used to unravel the physical mechanism behind the dynamics of successive accelerations experienced by a contact line through an array of pillars reported by [24, 28] where the local acceleration of the contact line can reach up to 100 times that of a spreading droplet on a smooth substrate. Such understanding and data are of primary importance for designing economical and low-energy consuming liquid transport devices, for example, in optimal designing of hemiwicking structures for heat-pipe wicks for improving the performance of lithium-ion batteries by structuring electrode surfaces [29].

Acknowledgment

This work was partially supported from Japan Society for the Promotion of Science (JSPS) by Grant-in-Aid for Challenging Exploratory Research (grant number: 16K14176) and by Grant-in-Aid for Scientific Research (grant number: 19H02083). Authors acknowledge a financial support from MAE (French Ministry of Foreign Affairs and International Development) as well as from JSPS through the PHC Sakura program 'Wetting dynamics in the presence of particles.' This work benefited from the support of the project FEFS ANR-CE21-2018 of the French National Research Agency (ANR).

Appendix

Validation of Laplace pressure measurement

Laplace pressure Δp_{gl} of a meniscus developing around a spherical particle is estimated from its profile in the $x - y$ plane, forms around the particle foot, as seen in Fig. 3 (b, c). The profile $x = \xi(y)$ of an axisymmetric meniscus

with a constant Laplace pressure is a solution of the Eqs. 4. Note that Δp_{gl} in Eqs. 4 is the average of the pressures at the meniscus surface $\xi(y)$ given by the following:

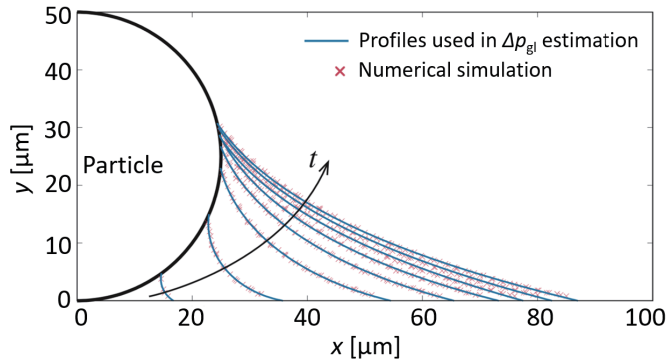

(a)

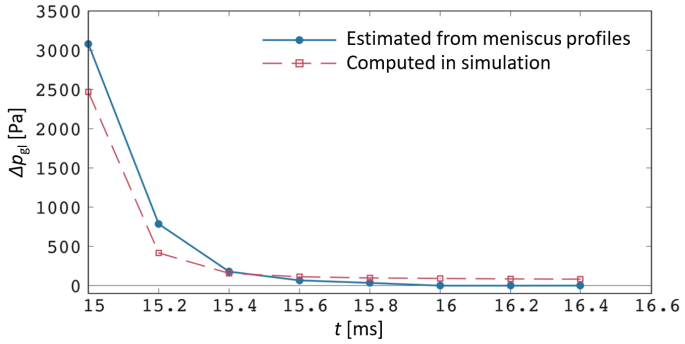

(b)

Figure A.1: (a) Profiles of a downstream side of meniscus developing around a spherical particle at t = 15, 15.2, 15.4, 15.6, 15.8, 16, 16.2, and 16.4 ms. Profiles determined in a numerical simulation and theoretical ones are compared. The latter profiles are used to estimate Laplace pressure Δp_{gl}. (b) Temporal variation of the pressure difference Δp_{gl} at gas-liquid interface of downstream side of meniscus by estimation based on Laplace pressure and simulation.

$$\Delta p_{\mathrm{gl}} = \frac{\sum_{n=2}^{N} \frac{1}{2}\left(x^{n-1}+x^{n}\right) s^{n} \cdot \frac{1}{2}\left(\Delta p_{\mathrm{gl}}^{n-1}+\Delta p_{\mathrm{gl}}^{n}\right)}{\sum_{n=2}^{N} \frac{1}{2}\left(x^{n-1}+x^{n}\right) s^{n}} \tag{5}$$

where $s^{n} = \sqrt{\left(x^{n}-x^{n-1}\right)^{2}+\left(y^{n}-y^{n-1}\right)^{2}}$, and (x^{n}, y^{n}) are the coordinates of a meniscus surface.

In order to compare the best fitting profiles and the results of numerical simulation, the profile obtained from the result of simulation using Eqs. 4 is overwritten again, and agree well as shown in Fig. A.1 (a). Figure A.1 (b) shows the comparison between the pressure at the gas-liquid interface by estimated from the profiles of Fig. A.1 (a) and computed by simulation. A slight decrease of Δp_{gl} with y is observed and trends are consistent. From the above, this Laplace pressure measurement is valid enough to indicate the relationship between the CL velocity and the pressure difference inside the meniscus, which are estimated by the meniscus profiles, in the experiment.

References

[1] L. Mu, D. Kondo, M. Inoue, T. Kaneko, H. N. Yoshikawa, F. Zoueshtiagh, I. Ueno, Sharp acceleration of a macroscopic contact line induced by a particle, Journal of Fluid Mechanics 830 (2017) R1.

[2] W. Barthlott, C. Neinhuis, Purity of the sacred lotus, or escape from contamination in biological surfaces, Planta 202 (1997) 1–8.

[3] H. Chen, P. Zhang, L. Zhang, H. Liu, Y. Jiang, D. Zhang, Z. Han, L. Jinag, Continuous directional water transport on the peristome surface of nepenthes alata, Nature 532 (2016) 85–89.

[4] D. L. Hu, J. W. M. Bush, Meniscus-climbing insects, Nature 437 (2005) 733–736.

[5] H. Jouhara, A. Chauhan, T. Nannou, S. Almahmoud, B. Delpech, L. C. Wrobel, Heat pipe based systems - advances and applications, Energy 128 (2017) 729–754.

[6] D. E. Kataoka, S. M. Troian, Patterning liquid flow on the microscopic scale, Nature 402 (1999) 794–797.

[7] B. L. Kessenich, N. Pokhrel, E. Nakouzi, C. J. Newcomb, M. Flury, L. Maibaum, J. J. D. Yoreo, Connecting wettability, topography, and chem-

istry in a simple lipid-montmorillonite system, Journal of Colloid and Interface Science 555 (2019) 498–508.

[8] K. M. Ang, L. Y. Yeo, Y. M. Hung, M. K. Tan, Graphene-mediated microfluidic transport and nebulization via high frequency rayleigh wave substrate excitation, Lab on a Chip 16 (2016) 3503–3514.

[9] S. Ross, P. Becher, The history of the spreading coefficient, Journal of Colloid and Interface Science 149 (2) (1992) 575–579.

[10] T. Young, An essay on the cohesion of fluids, Philosophical Transactions of the Royal Scociety of London 95 (1805) 65–87.

[11] R. L. Hoffman, A study of the advancing interface. i. interface shape in liquid-gas systems -, Journal of Colloid and Interface Science 50 (2) (1975) 228–241.

[12] J. Lopez, C. A. Miller, E. Ruckenstein, Spreading kinetics of liquid drops on solids, Journal of Colloid and Interface Science 56 (3) (1976) 460–468.

[13] L. H. Tanner, The spreading of silicone oil drops on horizontal surfaces, Journal of Physics D: Applied Physics 12 (1979) 1473–1484.

[14] A.-M. Cazabat, M. A. C. Stuart, Dynamics of wetting: effects of surface roughness, Journal of Physical Chemistry 90 (22) (1986) 5845–5849.

[15] R. N. Wenzel, Resistance of solid surfaces to wetting by water, Industrial and Engineering Chemistry 28 (8) (1936) 988–994.

[16] L. Courbin, E. Denieul, E. Dressaire, M. Roper, A. Ajdari, H. A. Stone, Imbibition by polygonal spreading on microdecorated surfaces, Nature Materials 6 (2007) 661–664.

[17] R. Xiao, E. N. Wang, Microscale liquid dynamics and the effect on macroscale propagation in pillar arrays, Langmuir 27 (2011) 10360–10364.

[18] N. Obara, K. Okumura, Imbibition of a textured surface decorated by short pillars with rounded edges, Physical Review E 86 (2012) 020601(R).

[19] J. Wang, M. Do-Quang, J. J. Cannon, F. Yue, Y. Suzuki, G. Amberg, J. Shiomi, Surface structure determines dynamic wetting, Scientific Reports 5 (2015) 8474.

[20] J. Kim, M.-W. Moon, H.-Y. Kim, Dynamics of hemiwicking, Journal of Fluid Mechanics 800 (2016) 57–71.

[21] D. Kondo, L. Mu, F. de Miollis, T. Ogawa, M. Inoue, T. Kaneko, T. Tsukahara, H. N. Yoshikawa, F. Zoueshtiagh, I. Ueno, Acceleration of the macroscopic contact line of a droplet spreading on a substrate after interaction with a particle, International Journal of Microgravity Science and Application 34 (4) (2017) 340405.

[22] R. G. Cox, The dynamics of the spreading of liquids on a solid surface. part 1. viscous flow, Journal of Fluid Mechanics 168 (1986) 169–194.

[23] L. Mu, H. N. Yoshikawa, D. Kondo, T. Ogawa, M. Kiriki, F. Zoueshtiagh, M. Motosuke, T. Kaneko, I. Ueno, Control of local wetting by microscopic particles, Colloids and Surfaces A 555 (2018) 615–620.

[24] L. Mu, H. N. Yoshikawa, F. Zoueshtiagh, T. Ogawa, M. Motosuke, I. Ueno, Quick liquid propagation on a linear array of micropillars, Langmuir 35 (2019) 9139–9145.

[25] C. W. Hirt, B. D. Nichols, Volume of fluid (vof) method for the dynamics of free boundaries, Journal of Computational Physics 39 (1981) 201–225.

[26] J. U. Brackbill, D. B. Kothe, C. Zemach, A continuum method for modeling surface tension, Journal of Computational Physics 100 (2) (1992) 335–354.

[27] A.-L. Biance, C. Clanet, D. Q. r , First steps in the spreading of a liquid droplet, Physical Review E 69 (2004) 016301.

[28] E. Spruijt, E. L. Guludec, C. Lix, M. Wagner, D. Quéré, Liquid filmification from menisci, Europhysics Letters 112 (2015) 16002.

[29] W. Pfleging, A review of laser electrode processing for development and manufacturing of lithium-ion batteries, Nanophotonics 7 (2018) 549–573.